Defense Technical Information Center Compilation Part Notice

ADP011827

TITLE: High Refractive Index Si/SiOx Based Nanocomposites

DISTRIBUTION: Approved for public release, distribution unlimited

HIGH REFRACTIVE INDEX Si/SiO_X BASED NANOCOMPOSITES

T. PHELY-BOBIN, D.E. BHAGWAGAR, F. PAPADIMITRAKOPOULOS*
Dept. of Chemistry, Polymer Science Program, Nanomaterials Optoelectronics Lab., Institute of Materials Science, University of Connecticut, Storrs, CT 06269

1. Introduction

Nanosized materials and their composites have generated enormous interest in recent years.[1-3] The need for high refractive index materials that readily conform to the elaborate structures proposed for photonic band-gap structures,[4,5] have attracted considerable attention in high loading nanocomposites.[6-8] The potential benefits in generating materials that gradually bridge the large refractive index gap between organics and inorganics along with maintaining reduced absorption and scattering, could benefit an array of photonic devices by improving the optical-coupling efficiencies between semiconductors and plastics or glass.[9] For example, the refractive indices of polymers vary between 1.3 and 1.7, while those of inorganic semiconductors vary between 2 and 5.[10] Some specialty polymers can exhibit refractive index greater than 2, such as poly(thiophene) with $n = 2.12$,[11] although this is strongly coupled to optical absorbance in the visible region. Inorganic high band-gap materials, such as TiO_2, could reach up to refractive indices of 2.9 in their crystalline state, but above this limit it is necessary to consider composites of inorganic semiconductors such as those presented in Table 1.[10]

TABLE 1. Refractive indices and absorption coefficients in the visible range for some of the ultra-high refractive index semiconductor inorganics

Material	Refractive Index (n)			Absorption Coefficient (k)		
	400 nm	500 nm	620 nm	400 nm	500 nm	620 nm
Crystalline Si	5.57	4.30	3.91	0.387	0.073	0.022
Amorphous Si	4.38	4.47	4.23	2.02	0.992	0.461
Ge	4.14	4.34	5.59	2.215	2.384	0.933
GaP	4.20Í	3.59	3.32	0.275	2.5×10^{-3}	2.8×10^{-7}
InP	4.42	3.82	3.55	1.735	0.511	0.317
PbS	3.62	4.35	4.19	2.015	2.238	1.773

High refractive index nanocomposites of PbS nanoparticles in gelatin or polyethylene oxide have been thoroughly investigated by Suter *et al.*[6-8] Their studies indicate that both PbS particle size and loading influence the overall refractive index of the nanocomposite. Very small particles show reduced refractive index as compared to that of particles with diameter equal or greater than 25 nm which approach the refractive index of bulk PbS.[8] The absorption coefficient of PbS nanoparticles showed similar

G.M. Chow et al. (eds.), Nanostructured Films and Coatings, 323–335.

nanoparticle-size behavior to that of refractive index. Based on their experimental data Suter *et. al.*[8] have shown that the overall refractive index of the nanocomposite n is to the first approximation proportional to the volume fractions v_i and refractive indices n_i of its components respectively ($n = n_1v_1 + n_2v_2$ for a two component system).

The technological challenges to achieve high refractive index inorganic-organic nanocomposites ($n > 2.5$) of increased transparency requires the use of high refractive index nanoparticles with low absorption coefficient in the visible range and diameter between 20 to 40 nm (well below one tenth of the wavelength of light (400-800 nm) in order to suppress Rayleigh scattering). For the same reasons, agglomerates and large sized scatterers, such as voids, should be scrupulously excluded. Based on the absorption coefficient of ultra-high refractive index inorganics listed at Table 1, GaP appears to be the material of choice with second to best crystalline Si[10]. When one incorporates the inherently low density and cost of Si along with various safety reasons of nanofabrication, Si and its nanocomposites overweighed the advantages of GaP.

Several preparation techniques for silicon nanoparticles have been reported such as chemical-vapor pyrolysis or deposition,[12-17] sputtering,[18-20] gas evaporation,[21] anodic etching,[22-26] and high-energy milling.[27] Electrochemical etching followed by electropolishing have been used to prepare porous silicon films of increased transparency with the index of refraction n calculated to be 2 in the IR.[28] Ultimately, high energy milling was chosen based on its environmental friendliness, low cost, and relative ease of nanoparticle separation. However this techniques introduces some limitation with respect to chemical purity and partial amorphization (which results in increased absorption, see Table 1) as a result of milling. This paper describes our current results on the characterization of these nanoparticles along with our recent attempts to fabricate high refractive index nanocomposites.

2. Results and Discussion

2.1. PREPARATION AND CHARACTERIZATION OF COLLOIDAL SILICON:

The profound technological importance of the silicon-based industry has stimulated considerable investigation into attaining well-controlled nanosized Si.[12-15,17-27,29] Recently, Shen *et.* al.[27] reported the use of high energy milling for nanosizing silicon in order to attain crystal grain sizes ranging from 3 to 20 nm. This has prompted us to employ this technique in order to produce nanosized Si, in large quantities, for the fabrication of high refractive index nanocomposites. Dispersing the freshly milled Si powder into solvents such as ethanol, water and tetrahydrofuran (THF) has resulted in black suspensions that quickly flocculate to leave a clear supernatant. Mild sonication has resulted in similar suspensions that require considerably longer time to settle down. Figure 1(a) indicates that high-energy nanomilling yields particles with very broad size distributions (3 to 500 nm), clearly unsuitable for use in photonic applications.

Significant effort was put into the extraction of Si nanoparticles with well defined average size (20 - 30 nm) and narrow size distributions. Several different methods were

employed to achieve separation including filtration and centrifugation. A series of trials were performed and parameters such as exposure to oxygen and sonication time and temperature were proven crucial. The formation of an ultra-thin silicon oxide that will be discussed later on in this paper appeared to be instrumental into stabilizing nanosilicon colloids.[12,13,17,26] Filtration of sonicated suspensions proved to be a less effective technique for separation of colloidal nanosilicon, highly likely due to the fact that small particles are attracted and halted during percolation through larger agglomerates. On the other hand, centrifugation quickly separates the large agglomerates from nanosilicon leaving a bright orange, lightly opalescent supernatant of colloidal Si. Optimization of

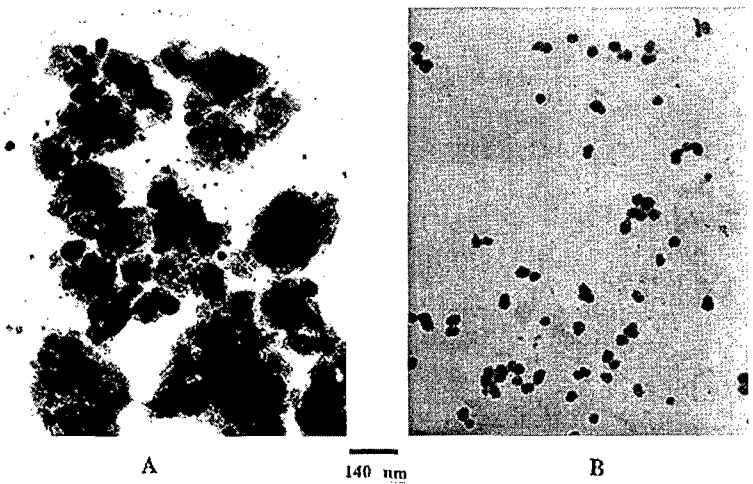

Figure 1. Transmission electron micrograph of Si, **(A)** as-milled, and **(B)** after separation by centrifugation

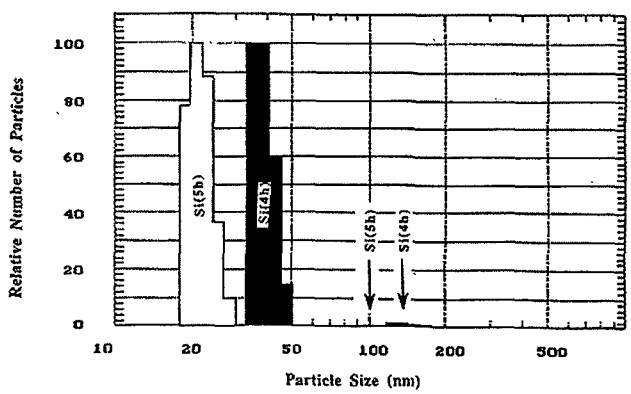

Figure 2. Number average particle size distribution obtained by dynamic light scattering from centrifuged colloidal Si suspensions as a function of milling time.

sonication temperature (c.a. 10 °C) and centrifugation time and speed (90 min. at 3000 rpm) has yielded colloidal Si with the desired average size and size distribution shown in Figure 1(b).

The average size of these nanoparticles, as determined by TEM was corroborated by size distribution analysis obtained by Dynamic Light Scattering (DLS) shown in Figure 2. For five hours milling time, the majority of nanoparticles lies between 20 and 30 nm (see Figure 1(b)). The correlation function obtained by DLS clearly does not obey Gaussian statistics. An alternative fitting procedure (Nicomp) developed especially for lightly agglomerated colloids (less than 1% agglomeration) has shown a near perfect fit based on a bimodal distribution shown in Figure 2. The small fraction of particles in the range between 100 to 150 nm sizes is present in all colloidal nanosilicon suspensions, even at very dilute concentrations. Based on the fact that microfiltration through 100 nm Nylon as well as Teflon filters has failed to remove these agglomerates, it is believed that they originate from a dynamic agglomeration - deagglomeration process slow enough to be measured by DLS. These agglomerates might look like those present in Figure 1(b), although considerable caution has to be exercised based on the markedly different nature of sample preparation (liquid vs. solid).

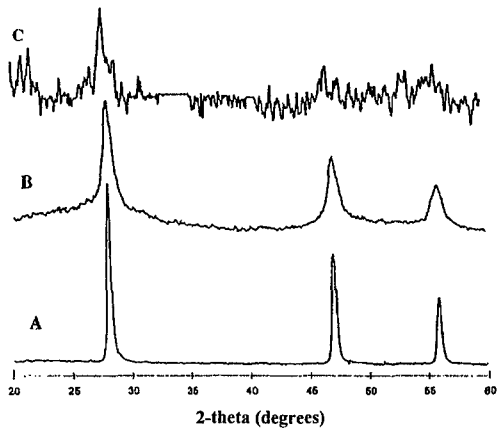

Figure 3. Radial X-ray diffraction profiles of **(A)** bulk Si, **(B)** as-milled sample Si, and **(C)** Si after separation by centrifugation.

The X-ray diffraction (XRD) profiles for bulk silicon, as-milled powder (before separation) and separated nanoparticles are presented in Figure 3. Line broadening is clearly the biggest difference between bulk silicon and as milled sample (Figure 3A and 3B respectively). This is in agreement with the thorough investigation of Shen *et* al.[27], on the high energy ball-milling of Si, where nanocrystalline grains of Si ranging from 3 to 20 nm were obtained, based on high resolution TEM and XRD line broadening analysis.[27] A combination of pressure induced amorphization and crystallite-refinement-induced amorphization was proposed to be responsible for this thermodynamically unfavorable process. The authors also verified that the partial

amorphous (c.a. 15%) character of the milled Si powder was distributed heterogeneously among the nanocrystalline portions while isolated nanocrystals were surrounded by a layer of amorphous silicon, surprisingly enough not oxidized by the adsorbed oxygen.[27] The XRD profile of the isolated nanosilicon in Figure 3C, although attained with significantly lower signal to noise ratio due to instrumentation shortcomings, resembles that of as milled powder with marginally increased line-broadening. Based on the work of Shen *et* al.[27], and the work presented below, it is currently believed that these nanoparticles consist of nanocrystalline Si interior with an amorphous Si exterior, partially coated with surface oxide which assists formation of colloidal suspensions in polar solvents.[12,13,26]

2.2. HIGH REFRACTIVE INDEX GELATIN NANOCOMPOSITES:

These Si nanoparticles were used to fabricate high refractive index nanocomposites, with refractive indices up to 3.2, when dispersed in gelatin.[30] Gelatin and poly(ethyleneoxide) have been extensively used for the fabrication of high refractive index nanocomposites with PbS.[6-8] The multiple functional sites in gelatin, a denatured protein, and its solubility in polar protic solvents such as water and ethanol makes it a matrix of choice for the fabrication of silicon based nanocomposites. Mixing an aqueous solution of gelatin with the ethanolic suspension of Si nanoparticles and concentrating by bubbling N_2, a viscous brown liquid was obtained. The color of this liquid offers a first indication that gelatin strongly interacts with the silicon nanoparticles and prevents them from agglomerating which would otherwise have resulted in a black, non transparent liquid. Low speed, slow acceleration spin coating results in high quality films (c.a. 30 - 50 nm) that are further densified by vacuum annealing at 150 °C.

2.3. SELF-ASSEMBLED Si/SiO_X NANOCOMPOSITES:

In an attempt to minimize concentration fluctuation, our research was recently shifted towards spontaneous nanoparticle adsorption on surfaces from dilute solutions. As it will quickly become apparent, this method offers significant advantages over highly filled systems for films below 1,000Å on various substrates such as glass, quartz, silver or gold.

The formation of stable Si colloids in polar solvents has been attributed to the growth of a thin surface oxide layer.[13,26,30,31] The thickness of such layer has been postulated to be particularly important to enable these relatively large particles to remain suspended,[30] although its minimum value is presently undetermined. With this in mind, a number of oxidizing agents were investigated to promote facile oxidation during sonication in EtOH. It was quickly recognized that when the moisture levels in 100% ethanol were kept low (H_2O concentration < 0.15 %), and sonication took placed in sealed containers, metastable Si colloids were produced that uniformly coat the inside wall of their glass container upon storage. The high energies achieved during sonication, apart from keeping the nanoparticles suspended in EtOH, also provide the means for performing chemistry, in the presence of oxidizing agents such as benzoyl peroxide or 3-

chloroperbenzoic acid.[32,33] A small amount of benzoyl peroxide (1.79×10^{-4} M) was found to produce the optimum results in terms of concentration of Si nanoparticles.

Scheme 1 illustrates the chemistry performed during sonication as analyzed by GC/MS of the silicon colloid and FTIR spectroscopy. The presence of benzoic acid, benzoylethyl ester and tetraethoxysilane (TEOS), along with unreacted benzoyl peroxide indicate that sonication can provide considerable amount of energy not only to perform chemical reactions, such as the cleavage of benzoyl peroxide, the formation of benzoic acid and benzoylethyl ester but also convert some of the milled Si to TEOS.

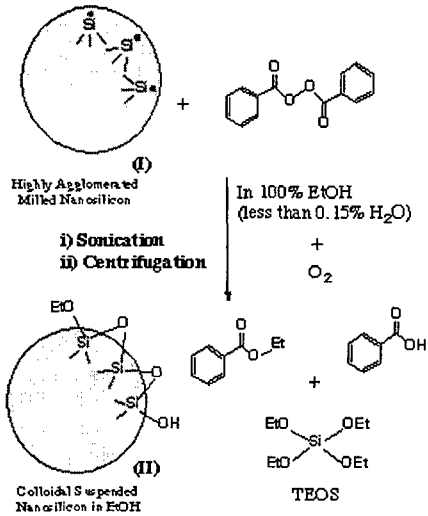

Scheme 1. Schematic representation of the sonication-assisted oxidation of silicon nanoparticles

Figure 4A illustrates the FTIR spectrum of silicon nanoparticles **(II)**, subjected to three consecutive centrifugation/decantation/resuspension cycles to remove all reactants and products of Scheme I that are non-bonded to nanoparticles. The underlying reactions of Scheme I facilitate the controlled release of H_2O which in turns slowly oxidizes the surface of the Si nanoparticles forming Si-OH and Si-O-Si groups.[34] The silanol (SiOH) groups are witnessed with two doublets centered around 3712 and 3612 cm^{-1} (associated with non-hydrogen bonded Si-O–H stretching) along with a much broader peak, centered around 3300 cm^{-1}, from the hydrogen bonded Si-O–H stretching. At present, the origin of the two clearly resolved Si-O–H doublets is not entirely understood. Parameters such as the degree of association (between the neighbor SiOH and SiOH/SiOEt groups), the number of OH substitutions (single vs. geminal OH groups), variety in fractured crystal planes during nanomilling, and the degree of surface oxidation could affect the spectral signature of the Si-O–H stretching mode.[35-37] The strong absorption envelop between 1170-1050 cm^{-1}, originates from Si–O–Si and Si–O–C stretching modes.[34,38] The shoulders at 1170 and 1055 cm^{-1} correspond to ethoxysiloxane (SiOEt) groups (1170 cm^{-1} for the CH_3 rocking absorption and 1055 cm^{-1}

for the Si–O-Si stretching of $Si(OEt)_n$ (n = 1,2,3) groups).[38] The strong absorptions associated with C–H stretching (between 2975 - 2850 cm^{-1}) and C–H deformation (five peaks between 1700 - 1300 cm^{-1}) are additional evidence for the presence of ethoxysiloxane groups on the surface of these nanoparticles.[37]

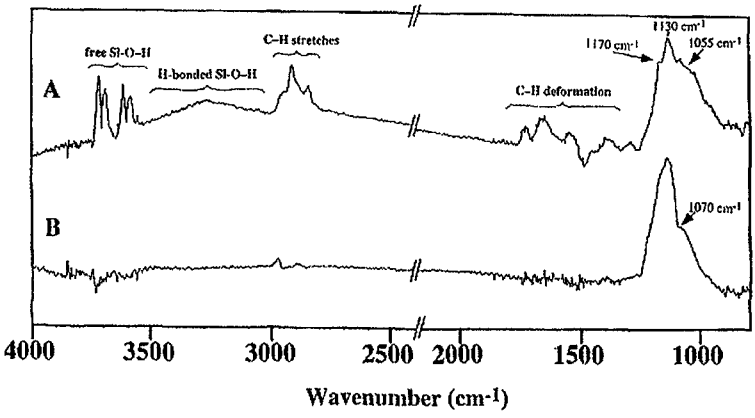

Figure 4. FTIR spectra of silicon nanoparticles **II** before **(A)** and after **(B)** their assembly on a SiO_2 coated (ca. 400 Å) double-polished silicon substrate. (See text for details)

The thermally grown oxide on the double polished silicon substrate allows these nanoparticles to self-assemble on both sides, resulting in highly uniform films. Figure 4B depicts the FTIR spectrum of a 12 hrs. grown film. The relatively strong adhesion of these nanoparticle assemblies to the substrate prevent them from been lifted-off during subsequent washing in fresh ethanol to remove all reactants and products of Scheme I that are non-bonded to these assemblies. The significant reduction of the shoulders at 1170 and 1055 cm^{-1} indicates the formation of SiO_x network (1030 and 1070 cm^{-1}) at the expense of the ethoxysiloxane groups.[39] This is also confirmed by the disappearance of both free and hydrogen bonded SiOH groups along with a dramatic reduction in absorbance of the C–H stretching (~2900 cm^{-1}) and C–H deformation (1700 - 1300 cm^{-1}) peaks.[40]

The formation of SiO_x network is strongly dependent on the pH of the ethanolic suspension.[41-43] The generation of benzoic acid (see Scheme 1) lowers the pH of the nanosilicon suspensions to 5.0 ± 0.5. At this range, the hydrolysis of TEOS and the ethoxysiloxane groups on the nanoparticles tends to be faster than the condensation of silanol groups to silica.[41,42] On the other hand, the surface oxidation of Si nanoparticles keeps the H_2O concentration in these suspensions sufficiently low which corroborates with the presence SiOEt groups at this pH (see Figure 4A). In addition, at pH of 5, the partial protonation of the ethoxysiloxane groups decorates these nanoparticles with a positive surface charge, which contributes to the stability of their suspensions.[42,43] Upon immersion of a fresh silica surface (glass or quartz substrates) in these suspensions, the following mechanisms are set in gear.

(i) The weaker nucleophilicity of SiOH and SiOSi groups (present at the surface of glass or quartz substrates) versus the SiOEt groups (on the nanoparticles) makes these substrates less prone to protonation at pH of 5.[42,43] This offers a plausible mechanism that accounts why nanoparticles of **(II)** are not repelled away from the surface of these substrates.

(ii) Upon substrate-nanoparticle contact, the slow condensation of silanol groups results in the formation of SiOSi bridges and generation of additional H_2O. At pH of 5, this H_2O will further promote the fast hydrolysis of SiOEt groups (from nanoparticles as well as TEOS) to SiOH groups, eventually to yield a SiO_x matrix around the nanoparticles.[41-43] This is further corroborated by the complete elimination of the Si-O–H stretching in Figure 4B, which creates the slightly negative free Si-O–H absorption (~ 3735 cm^{-1}) as a result of substrate SiOH groups, which participate to this condensation (note that the FTIR spectra of double polished $SiO_2/Si/SiO_2$ wafers were included into the spectrometer's background).[38]

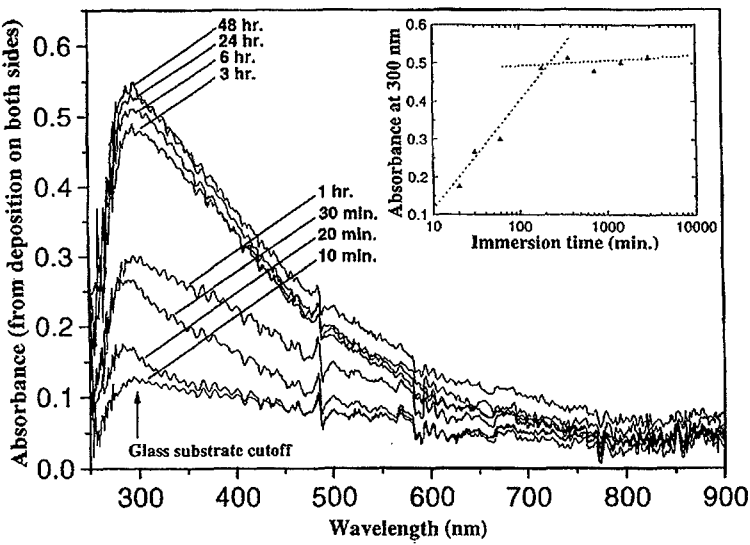

Figure 5. UV-vis absorption spectra of self-assembled Si/SiO_x nanocomposites on both sides of glass substrates as a function of immersion time in a colloidal suspension of **(II)**.

Figure 5 illustrates the UV-VIS absorption spectra of the adsorbed Si/SiO_x nanocomposite on glass substrates as a function of immersion time in a colloidal suspension of **(II)**. The rapid initial adsorption of this nanocomposite slows beyond 3 hours immersion time, revealing what appears to be a self-limiting deposition process. The optical quality and uniformity of such deposits are impressive, providing a nearly scatter-free coating on glass and quartz substrates. However, after 12 hours of immersion time, this coating begins to exhibit some scattering, which can be witnessed at the red spectral portion of Figure 5.

2.4. RAMAN CHARACTERIZATION OF Si/SiO_X NANOCOMPOSITES:

Raman spectroscopy has been shown to be suitable technique to study Si morphology.[44-46] Room temperature micro-Raman spectra were recorded on a Renishaw ramanoscope system equipped with a microscope attachment, in which the laser spot size could be focused to 1 mm in diameter (x100 objective), and with a power output of 35 mW. The excitation source was a 514.5-nm line of an argon ion laser. Figure 6 A illustrates the Raman spectrum of the starting polycrystalline Si powder (325-mesh size) as obtained from Alfa Aesar, with its equivalent XRD-spectrum illustrated in Figure 3A. Table 2 indicates that this is microcrystalline Si sample (*c*-Si = 511 cm^{-1})

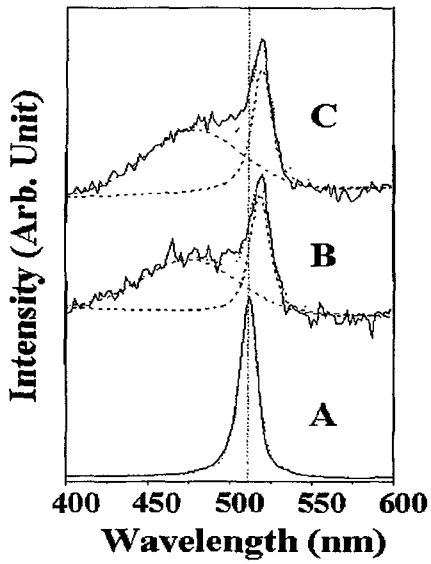

Figure 6. Room temperature Raman spectra of **(A)** mesh silicon, **(B)** as-milled Si, and **(C)** self-assembled Si/SiO_x nanocomposites on a gold substrate.

TABLE 2. Raman peak values as determined by a Gaussian-Lorenzian fit of the Figure 6 spectra.

Material/Process	*c*-Si component			*a*-Si component		
	peak center cm^{-1}	FWHM* cm^{-1}	Relative Area	peak center cm^{-1}	FWHM* cm^{-1}	Relative Area
325-mesh polycrystalline Si powder†	511 ± 2	12 ± 1	c.a. 100%			
as-milled Si sample (5 hrs in inert atmosphere)	518 ± 2	14 ± 1	c.a. 36%	475 ± 2	67 ± 2	c.a. 64%
self-assembled Si/SiO_x nanocomposites on gold	519 ± 2	12 ± 1	c.a. 30%	480 ± 2	69 ± 2	c.a. 70%

* FWHM stands as full-width at half maximum.
† Obtained from Alfa-Aesar, (99.5% nominal purity).

with a nearly undetectable amorphous components. Raman shifts between 505 and 513 cm^{-1} for crystalline Si have been reported by Kamiya *et al.*[44] A 512 cm^{-1} centered Raman peak for microcrystalline Si phase is due to TO phonons confined in microcrystals with diameter of several hundred angstroms. Iqbal and Veprek have shown that the peak frequency decreases from the single crystal value of 520 cm^{-1} to 512 cm^{-1} for a crystallite size of 35 Å.[45]

Figure 6B depicts the Raman spectrum of the as-milled Si (5 hours in inert atmosphere). Please note that the sample were exposed to air during the collection of its Raman spectrum as well as its equivalent XRD spectrum illustrated in Figure 3B. The broad *a*-Si Raman line, peaking at 475 cm^{-1} indicates considerable amorphization as a result of high-energy milling as reported by Shen *et al.*[27] and concurred by the significant line broadening shown in Figure 3. Contrary to the expected, the 518 cm^{-1} *c*-Si Raman peak indicates a pressure induced crystallite-refinement, also witnessed by Shen *et al.*[27] This was explained on the basis of elevated temperatures reached during high energy milling causing a small fraction of the crystals to grow to more perfect crystallites which are responsible for the up-shift of *c*-Si Raman peak to higher frequencies.

Olego *et al.*[46] proposed a model of the microcrystalline structure of annealed SiO_x semi-insulating polycrystalline silicon (SIPOS) films grown by low-pressure chemical vapor deposition. Based on Olego's model and corroborating unreported X-ray Photoelectron Spectroscopy data, these Si/SiO_x nanoparticles appear to have a nanocrystalline Si interior, coated with an amorphous Si shell, quite amenable for sonication assisted oxidation.

3. References

1. Klabunde, K.J. (1994)*Free atoms, clusters, and nanoscale particles,* Academic Press, San Diego.
2. Moser, W.R. (1996)*Advanced catalysts and nanostructured materials: modern synthetic methods,* Academic Press, San Diego.
3. Hoch, H.C., Jelinski, L.W. and Craighead, H.G. (1996)*Nanofabrication and biosystems: integrating materials science, engineering and biology,* Cambridge University Press, Cambridge.
4. Busch, K. and John, S. (1998) Photonic Band Gap Formation in Certain Self-Organizing Systems, *Physical Review E* **58**, 3896.
5. Joannopoulos, J.D., Meade, R.D. and Winn, J.N. (1995)*Photonic Crystals: Molding the Flow of Light,* Princeton University Press, Princeton, NJ.
6. Weibel, M., Caseri, W., Suter, U.W., Kiess, H. and Wehrli, E. (1991) Preparation of Polymer Nanocomposites with "Ultrahigh" Refractive Index, *Polymers for Advanced Technologies* **2**, 75-80.
7. Zimmermann, L., Weibel, M., Caseri, W. and Suter, U.W. (1993) High refractive index films of polymer nanocomposites, *J. Mater. Res.* **8**, 1742.

8. Kyprianidou-Leodidou, T., Caseri, W. and Suter, U.W. (1994) Size Variation of PbS Particles in High-Refractive-Index Nanocomposites, *J. Phys. Chem.* **98**, 8992.
9. Kitai, A.H. (1993)*Solid State Luminescence,* Chapman & Hall, London.
10. Palik, E.D. (1985)*Handbook of Optical Constants of Solids,* Academic Press, Orlando.
11. Sugiyama, T., Wada, T. and Sasabe, H. (1989) Optical nonlinearity of conjugated polymers, *Synth. Metals* **28**, C323.
12. Fojtik, A., Weller, H., Fiechter, S. and Henglein, A. (1987) Preparation of Colloidal Silicon and Preliminary Photochemical Experiments, *Chemical Physics Letters* **134**, 477.
13. Littau, K.A., Szajowski, P.J., Muller, A.J., Kortan, A.R. and Brus, L.E. (1993) A luminescent silicon nanocrystal colloid via a high-temperature aerosol reaction, *J. Phys. Chem.* **97**, 1224.
14. Takagi, H., Ogawa, H., Yamazaki, Y., Ishizaki, A. and Nakagiri, T. (1990) Quantum size effects on photoluminescence in ultrathin Si particles, *Appl. Phys. Lett.* **56**, 2379.
15. Rueckschloss, M., Ambacher, O. and Veprek, S. (1993) Structural aspects of light emitting nc-Si prepared by plasma CVD, *J. Lumin* **57**, 1.
16. Zhang, D. *et al.* (1994) Light emission from thermally oxidized silicon nanoparticles, *Appl. Phys. Lett.* **65**, 2684.
17. Nakajima, A., Sugita, Y., Kawamura, K., Tomita, H. and Yokoyama, N. (1996) Microstructure and Optical Absorption Properties of Silicon Nanocrystals Fabricated with Low Pressure Chemical Vapor Deposition, *J. Appl. Phys.* **80**, 4006.
18. Furukawa, S. and Niyasato, T. (1988) Quantum size effects on optical band gap of microcrystalline Si:H, *Phys. Rew. B* **38**, 5726.
19. Osaka, Y., Tsunetomo, K., Toyomura, F., Myoren, H. and Kohno, K. (1992) Visible photoluminescence from Si microcrystals embedded in silica glass films, *Jpn. J. Appl. Phys.* **31**, L365.
20. Sun, Y., Nishitani, R. and Miyasato, T. (1994) Study of hydrogen ion bombardement effect on the growth of Si:H films prepared by hydrogen plasma sputtering of silicon, *Jpn. J. Appl. Phys.* **33**, L1645.
21. Morisaki, H., Ping, F.W., Ono, H. and Yazawa, K. (1991) Above-band-gap photoluminescence from silicon fine particles with oxide shell, *J. Appl. Phys.* **70**, 1869.
22. Canham, L.T. (1990) Silicon quantum wire array fabrication by electrochemical and chemical dissolution, *Appl. Phys. Lett.* **57**, 1046.
23. Lehmann, V. and Gösele, U. (1991) Porous silicon formation: a quantum wire effect, *Appl. Phys. Lett.* **58**, 856.
24. Nakajima, A., Itakura, T., Watanabe, S. and Nakayama, N. (1992) Photoluminescence of porous silicon, oxidized then deoxidized chemically, *Appl. Phys. Lett.* **61**, 46.
25. Heinrich, J.L., Curtis, C.L., Credo, G.M., Kavanagh, K.L. and Sailor, M.J. (1992) Luminescent Colloidal Silicon Suspensions from Porous Silicon, *Science* **255**, 66.
26. Bley, R.A., Kauzlarich, S.M., Davis, J.E. and Lee, H.W.H. (1996) Characterization of Silicon Nanoparticles prepared from porous Silicon, *Chem. Mater.* **8**, 1881.

27. Shen, T.D. *et al.* (1995) The structure and property characteristics of amorphous/nanocrystalline silicon produced by ball milling, *J. Mater. Res.* **10**, 139.
28. Behren, J.v., Tsybeskov, L. and Fauchet, P.M. (1995) Preparation and Characterization of Utrathin porous Silicon Films, *Appl. Phys. Lett.* **66**, 1662.
29. Zhang, C. *et al.* (1994) Blue electroluminescent diodes utilizing blends of poly(p-phenylene vinylene) in poly(9-vinylcarbazole), *Synthetic Metals* **62**, 35.
30. Papadimitrakopoulos, F., Wisniecki, P. and Bhagwagar, D.E. (1997) Mechanically Attrited Silicon For High Refractive Index Nanocomposites., *Chem. Mat.* **9**, 2928.
31. Bhagwagar, D.E., Wisniecki, P. and Papadimitrakopoulos, F. (1997) Characterization of Nanosized Silicon Prepared by Mechanical Attrition for High Refractive Index Nanocomposites, *Mat. Res. Soc. Symp. Ser.* **457**, 439.
32. Suslick, K.S., Fang, M. and Hyeon, T. (1996) Sonochemical Synthesis of Iron Colloid, *J. Am. Chem. Soc.* **118**, 11960.
33. Suslick, K.S., Hyeon, T. and Fang, M. (1996) Nanostructured Materials Generated by High-Intensity Ultrasound: Sonochemical Synthesis and Catalytic Studies, *Chem. Mater.* **8**, 2172.
34. Liao, W.S. and Lee, S.C. (1996) Water-Induced room-temperature Oxidation of Si-H and -Si-Si- bonds in Silicon Oxide, *J. Appl. Phys.* **80**, 1171.
35. Mawhinney, D.B., Glass, J.A. and Yates, J.T. (1997) FTIR Study of the Oxidation of Porous Silicon, *J. Phys. Chem. B.* **101**, 1202.
36. Hoffmann, P. and Knozinger, E. (1987) Novel Aspects of Mid and Far IR Fourier Spectroscopy Applied to Surface and Adsorption Studies on SiO2, *Surface Science* **188**, 181-198.
37. Tedder, L.L., Lu, G. and Crowell, J.E. (1991) Mechanistic Studies of Dielectric Thin Film Growth by Low Pressure Chemical Vapor Deposition: The Reaction of Tetraehoxysilane with SiO2 Surfaces, *J. Appl. Phys.* **69**, 7037.
38. Deshmukh, S.C. and Aydil, E.S. (1995) Investigation of SiO2 Plasma Enchanced Chemical Vapor Deposition Through Tetraethoxysilane Using Attenuated Total Reflection Fourier Transform Infrared Spectroscopy, *J. Vac. Sci. Technol.* **A 13**, 2355.
39. Ishii, K., Ohki, Y. and Nishikawa, H. (1994) Optical Characteristics of SiO2 Formed by Plasma-enhanced Chemical-Vapor Deposition of Tetraethoxysilane, *J. Appl. Phys.* **76**, 5418.
40. Bao, T.I., Wu, M.S. and I., L. (1995) Infrared Studies of Room Temperature Deposition of Hydrogenated Silicon Oxide Films in RF Magnetron Discharges, *J. Appl. Phys.* **78**, 3342.
41. Keefer, K.D. (1990) Structure and Growth of Silica Condensation Polymers, in Zeigler, J. M. & Gordon-Fearon, F. W. (eds.), *Silicon-Based Polymer Science; A Comprehenive Resourse*, ACS, Washington, **224**, 227-240.
42. McNeiil, K.J., DiCaprio, J.A., Walsh, D.A. and Pratt, R.F. (1980) Kinetics and Mechanism of Hydrolysis of a Silicate Triester, Tri(2-methoxyethoxy)phenylsilane, *J. Am. Chem. Soc.* **102**, 1859.
43. Pohl, E.R. and Osterholtz, F.D. (1983) Kinetics and Mechanism of Aqueous Hydrolysis and Condensation of Alkyltrialkoxysilanes, in Ishida, H. & Kumar, G.

(eds.), *Molecular Characterization of Composite Interfaces*, Plenum Press, New York, **27**.

44. Kamiya, T., Kishi, M., Ushirokawa, A. and Katoda, T. (1981) Observation of the amorphous-to-crystalline transition in silicon by Raman scattering, *Appl. Phys. Lett.* **38**, 377.
45. Iqbal, Z. and Veprek, S. (1982) Raman scattering from hydrogenated microcrystalline and amorphous silicon, *J. Phys. C: Solid State Phys.* **15**, 377.
46. Olego, D.J. and Baumgart, H. (1987) Semi-insulating polycrystalline Si thinn films, *J. Appl. Phys.* **63**, 2669.